*J. Fluid Mech.* (2011), *vol.* 668, *pp.* 363–383. © Cambridge University Press 2010
doi:10.1017/S0022112010004763

# A numerical investigation of the propulsion of water walkers

PENG GAO[1] AND JAMES J. FENG[1,2]†

[1]Department of Chemical and Biological Engineering, University of British Columbia,
Vancouver, BC V6T 1Z3, Canada

[2]Department of Mathematics, University of British Columbia, Vancouver,
BC V6T 1Z2, Canada

(Received 8 February 2010; revised 6 September 2010; accepted 12 September 2010;
first published online 30 November 2010)

This paper presents a finite-element simulation of the interfacial flow during propulsion of water walkers such as fishing spiders and water striders. The unsteady stroke of the driving leg is represented by a two-dimensional cylinder moving on a specified trajectory. The interface and the moving contact lines are handled by a diffuse-interface model. We explore the mechanism of thrust generation in terms of the interfacial morphology and flow structures. Results show that the most important component of the thrust is the curvature force related to the deformation of the menisci and the asymmetry of the dimple. For water walkers with thick legs, the pressure force due to the inertia of the water being displaced by the leg is also important. The viscous force is negligible. An extensive parametric study is performed on the effect of leg velocity, stroke depth, leg diameter and surface wettability. The propulsive force is insensitive to the contact angle on the leg. However, the hydrophobicity of the leg helps it detach from the surface during the recovery stroke and thus decreases the resistance. It is also important for averting or delaying penetration of the interface at large rowing velocity and depth. In two dimensions, surface waves are more efficient than vortices in transferring the momentum imparted by the leg to the water.

**Key words:** contact lines, interfacial flows (free surface), propulsion

## 1. Introduction

Water striders and fishing spiders are small creatures living on water. Their legs are covered by a layer of micro-setae with nanoscale texture (Gao & Jiang 2004; Hu & Bush 2010), which renders the legs highly non-wetting or super-hydrophobic so that these creatures can stand effortlessly on water. Moreover, they can move quickly on water by rowing their legs on the surface. This amazing ability has attracted substantial research work (Bush & Hu 2006; Bush, Hu & Prakash 2007). The exploration of the underlying mechanism not only supplies a better understanding of nature but also has potential biomimetic applications (Hu, Chan & Bush 2003; Hu *et al.* 2007; Song & Sitti 2007). While the static problem of standing on water is well understood, the dynamic mechanism of propulsion is not. This paper seeks to address the outstanding issues from detailed computations of the fluid flow.

---

† Email address for correspondence: jfeng@math.ubc.ca

When a water walker stands on water, its hydrophobic legs push the water surface down to form dimples. The width of the dimple is characterized by a capillary length $\ell_c = \sqrt{\sigma/(\rho_1 - \rho_2)g} \approx 2.7\,\mathrm{mm}$, which is typically much larger than the leg radius. Here $\sigma$ is the surface tension; $\rho_1$ and $\rho_2$ are the densities of water and air, respectively; and $g$ is the gravitational acceleration. The weight of the insect is supported by a combination of buoyancy and curvature forces, the latter being the vertical component of the surface tension at the contact line. It can be demonstrated by using an extended Archimedes principle (Mansfield, Sepangi & Eastwood 1997; Keller 1998) that the curvature force is equal to the weight of water displaced beyond the contact line. Thus, the total supporting force is equal to the weight of water displaced by the leg and the dimple together. For real water striders whose legs are very thin ($\sim 100\,\mu\mathrm{m}$), the curvature force supports most of the weight. Vella, Lee & Kim (2006) demonstrated that the maximum load that can be supported by thin cylinders becomes independent of the contact angle when it exceeds $\pi/2$. Therefore, the super-hydrophobicity of the leg does not necessarily improve its load-bearing capability on water (Song & Sitti 2007).

The dynamic propulsion of water walkers is much more complex than the static flotation. On the basis of observations, three propulsion mechanisms have been proposed so far: *wave drag*, *form drag* and *momentum transfer by vortices*. When a water walker rows its legs, surface ripples are generated. These capillary–gravity waves propagate backward to the far field, presumably carrying the momentum away from the insect. This amounts to a wave drag on the rowing leg, thereby giving the leg a forward thrust (Anderson 1976; Denny 1993; Sun & Keller 2001). This explanation was widely accepted at the beginning, partly because the surface waves were the only flow structure visible to the naked eye. However, this picture was apparently complicated by Denny's paradox (Denny 1993, 2004; Suter *et al.* 1997; Hu *et al.* 2003). According to linear wave theory, there exists a minimum wave speed $c_{min} = \sqrt[4]{4\sigma g/\rho_1} = 23\,\mathrm{cm\,s^{-1}}$ (Lamb 1932). In order to generate waves and hence wave drag, the leg must move at least as fast as $c_{min}$, which is a feat that certain smaller water-walking creatures, such as infant striders, are incapable of (Denny 1993). That infant water striders do move constitutes the paradox. Towards its resolution, Hu (2006) and Hu & Bush (2010) pointed out that the $c_{min}$ criterion is based on *steady* wave theory (Raphaël & de Gennes 1996; Sun & Keller 2001) and thus does not apply to the unsteady strokes of real water walkers. Bühler (2007) further demonstrated that the impulsive start of a point force near an air–water interface does generate unsteady waves.

Motivated by the paradox, Suter *et al.* (1997) carried out experiments in which a segment of the leg of the fishing spider *Dolomedes triton* was dragged on water at a constant velocity below $c_{min}$. No waves were generated, and thus the wave drag was absent. They measured the force on the leg and found that it can be largely accounted for by the drag force on a half-cylinder that represents the 'leg-cum-dimple', i.e. the leg plus the deformed meniscus. Although this drag may contain viscous friction, their key idea is that the form drag on the meniscus, of a much larger area than the leg, allows a much larger thrust than can be produced on the leg surface alone. Thus, this has been called the form drag mechanism for propulsion (Bush & Hu 2006). Of course, this mechanism is wave-independent and does not involve Denny's paradox.

More recently, Hu *et al.* (2003) and Hu & Bush (2010) performed careful experimental observations of the wake produced by the water strider *Gerris remigis* as well as fishing spiders. They found capillary waves being generated by even infant water striders. More importantly, the driving legs shed hemispherical *vortex pairs* in the water that travel backward at a characteristic speed of $4\,\mathrm{cm\,s^{-1}}$. The horizontal momentum carried by these vortices is estimated to be comparable to that of the strider. Thus, Hu *et al.* (2003) concluded that the leg imparts momentum to water primarily through these vortex dipoles, while the waves are a mere by-product of the stroke. The vortex scenario is attractive, since coherent vortex structures have long been recognized as the dominant mechanism of locomotion for fish and birds (e.g. Dickinson 2003). For water walkers, however, the interface is implicated in the vortex generation, and its role remains to be elucidated.

Note that these three mechanisms were proposed from different perspectives. They are not mutually exclusive, nor do they include all the relevant dynamics. The main objective of our study is to reconcile these proposals by elucidating the detailed flow structures responsible for each. This will provide answers to several important questions. For instance, what is the relationship among the different mechanisms? What is the effect of the leg hydrophobicity on the locomotion? How can a water walker boost its propulsion? Tackling these questions requires an appropriate model for the leg stroke, as well as a quantitatively accurate description of the interfacial shape and the flow field. Hence we resort to direct numerical computations.

We will present two-dimensional (2-D) numerical simulations of the locomotion of water walkers by rowing. We employ an unsteady model of the stroking cycle of the leg with a finite duration, which is more realistic than previous steady-state (Suter *et al.* 1997; Sun & Keller 2001) or impulsive-point-force models (Bühler 2007). The moving surface and moving contact lines are handled by a diffuse-interface model, and the numerical solution uses finite elements on an unstructured grid with adaptive meshing. The main contribution of our paper is a clear analysis of the propulsion mechanism in terms of the hydrodynamic forces on the leg, accounting for all of the factors including surface tension, viscosity, pressure and fluid inertia. This not only allows a quantitative prediction of the propulsive force but also demonstrates the relative importance of waves and vortices to different stages of the propulsion.

## 2. Physical model and numerical method

Since water walkers propel themselves by rowing their middle legs, only the flow produced by these propulsive legs is considered. To simplify the problem, the leg is modelled as a 2-D solid cylinder, without taking into account the complex microstructures of the leg surface (Gao & Jiang 2004; Bush *et al.* 2007). In particular, Hu & Bush (2010) have noted that the anisotropy of the integument and the contact-angle hysteresis contribute to the locomotion. Our simple model omits such effects and reflects only the hydrophobicity of the leg by a large contact angle $\theta$. Air and water are treated as a stratified two-phase system, both components being incompressible and Newtonian. The lower fluid (water) has density $\rho_1$ and viscosity $\mu_1$ and the upper one (air) $\rho_2$ and $\mu_2$.

The decision to use a 2-D model is mostly based on the lower computational cost. Then its relevance to three-dimensional (3-D) reality needs to be justified. Experimental pictures show that where the leg of a water walker touches the water surface, it is largely parallel to the water surface and makes a horizontal dimple (Suter *et al.* 1997; Suter & Wildman 1999; Hu *et al.* 2003). If the dimple is much longer than the capillary length $\ell_c = 2.7\,\mathrm{mm}$, the 3-D end effect is negligible, and the process can be treated as 2-D. This is the case for adult water striders and fishing spiders, which typically have a leg length of 1.5 cm in contact with water (Suter *et al.* 1997; Hu & Bush 2010). During rowing, a 3-D end vortex may arise at the distal end of

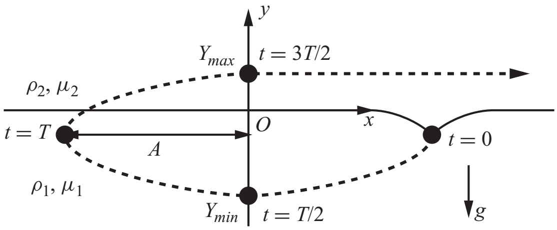

FIGURE 1. Schematic illustration of the leg movement. The solid and dashed curves denote the initial interface and the leg trajectory, respectively.

the leg, especially if it is submerged. This vortex grows in time $t$, and its size can be estimated from the density $\rho_1$ and viscosity $\mu_1$ of water as $\sqrt{\mu_1 t/\rho_1}$. The duration of a stroke is typically less than 0.1 s, which gives a vortex size below 0.3 mm. This is again negligible in comparison with the length of the dimple. Three-dimensionality becomes important for infant water striders having short legs and for long-time growth of 3-D vortices in the wake of the insect (Hu *et al.* 2003). The latter is related to the transfer of momentum by vortices. These scenarios cannot be accounted for by our model, and we will revisit this issue in § 3.3.

Only limited information on the leg stroke is available. Suter *et al.* (1997) measured the typical velocity of the driving leg of fishing spiders. But the exact trajectory of the leg is unavailable for most water walkers. For simplicity and generality, we will use the following idealized leg stroke. In a stationary reference frame in which the unperturbed fluid interface is at $y = 0$ (figure 1), we prescribe the trajectory of the leg $(X(t), Y(t))$ by

$$X(t) = \begin{cases} A\cos\dfrac{\pi t}{T} & \text{for} \quad t \leqslant \dfrac{3T}{2}, \\ \dfrac{\pi A}{T}\left(t - \dfrac{3T}{2}\right) & \text{for} \quad t > \dfrac{3T}{2}, \end{cases} \tag{2.1}$$

$$Y(t) = \begin{cases} -\dfrac{1}{2}(Y_{max} - Y_{min})\sin\dfrac{\pi t}{T} + \dfrac{1}{2}(Y_{max} + Y_{min}) & \text{for} \quad t \leqslant \dfrac{3T}{2}, \\ Y_{max} & \text{for} \quad t > \dfrac{3T}{2}. \end{cases} \tag{2.2}$$

The motion of the leg is thus composed of a backward driving stroke with duration $T$ and a recovery stroke, as illustrated in figure 1. Here, $2A$ is the horizontal displacement of the leg during the driving stroke; $Y_{max}$ and $Y_{min}$ are the maximum and minimum vertical positions of the leg, respectively. Initially, the leg is located at $(x_0, y_0) = (A, (Y_{max} + Y_{min})/2)$. Only one stroke is studied, and the simulation typically ends at $2T \sim 2.5T$. The driving stroke generates the propulsive force, and the long-time behaviour $(t \gg T)$ is not of present interest.

We use a diffuse-interface method to handle the interfacial deformation and the moving contact line (Jacqmin 2000; Qian, Wang & Sheng 2006; Yue, Zhou & Feng 2010). We view the air–water interface as a thin diffuse layer of non-zero thickness, within which the two fluids mix to store a mixing free energy. A phase-field variable $\phi$ is introduced such that $\phi = 1$ in the water and $\phi = -1$ in the air. Further, $\phi$ varies in a steep and smooth way across the interface, which is given by the level set $\phi = 0$.

The evolution of $\phi$ is governed by the advective Cahn–Hilliard equation

$$\frac{\partial \phi}{\partial t} + \boldsymbol{v} \cdot \nabla \phi = \nabla \cdot (\gamma \nabla G), \tag{2.3}$$

where $G = \lambda[-\nabla^2 \phi + (\phi^2 - 1)\phi/\epsilon^2]$ is the bulk chemical potential; $\gamma$ is the mobility and $\boldsymbol{v} = (u, v)$ is the velocity vector; $\lambda$ is the mixing energy density and $\epsilon$ is the capillary width characterizing the thickness of the diffuse interface. On the basis of a one-dimensional equilibrium profile of $\phi$, $\lambda$ and $\epsilon$ are related to the classical interfacial tension $\sigma$ by

$$\sigma = \frac{2\sqrt{2}}{3}\frac{\lambda}{\epsilon}. \tag{2.4}$$

The flow is governed by the continuum and momentum equations

$$\nabla \cdot \boldsymbol{v} = 0, \tag{2.5}$$

$$\rho\left(\frac{\partial \boldsymbol{v}}{\partial t} + \boldsymbol{v} \cdot \nabla \boldsymbol{v}\right) = -\nabla p + \nabla \cdot [\mu(\nabla \boldsymbol{v} + (\nabla \boldsymbol{v})^{\mathrm{T}})] + G\nabla\phi - \rho g \boldsymbol{j}, \tag{2.6}$$

where $\boldsymbol{j}$ is the upward unit vector. The density $\rho$ and viscosity $\mu$ are defined as

$$\rho = \tfrac{1}{2}(1+\phi)\rho_1 + \tfrac{1}{2}(1-\phi)\rho_2, \tag{2.7}$$

$$\mu = \tfrac{1}{2}(1+\phi)\mu_1 + \tfrac{1}{2}(1-\phi)\mu_2. \tag{2.8}$$

Note that the momentum equation has an additional term $G\nabla\phi$, representing the body force normal to the interface generated by the interfacial tension.

In the far field, the Cahn–Hilliard equation is supplemented by the following boundary conditions: $\boldsymbol{n} \cdot \nabla G = 0$ and $\boldsymbol{n} \cdot \nabla \phi = 0$, $\boldsymbol{n}$ being the outward unit normal vector. For the Navier–Stokes equations we impose vanishing stress at the upper boundary and vanishing velocity elsewhere on the outer boundary. On the surface of the solid cylinder, we employ the following no-slip, no-flux and contact-angle boundary conditions:

$$\boldsymbol{v} = (X'(t), Y'(t)), \tag{2.9}$$

$$\boldsymbol{n} \cdot \nabla G = 0, \tag{2.10}$$

$$\lambda \boldsymbol{n} \cdot \nabla \phi + f_w'(\phi) = 0. \tag{2.11}$$

The contact angle enters through the wall free energy $f_w$, which is postulated as (Jacqmin 2000; Yue *et al.* 2010)

$$f_w(\phi) = -\sigma \cos\theta \frac{\phi(3-\phi^2)}{4} + \frac{\sigma_{w1} + \sigma_{w2}}{2}, \tag{2.12}$$

where $\sigma_{w1}$ and $\sigma_{w2}$ are respectively the wall energies of water and air, related to the contact angle by Young's equation $\sigma_{w2} - \sigma_{w1} = \sigma \cos\theta$. The condition (2.11) assumes that the contact line is always in equilibrium with the wall, and both the advancing and receding contact angles are the same as the static contact angle. This precludes a possible propulsion mechanism associated with contact-angle hysteresis (Hu & Bush 2010). In the diffuse-interface formalism, the air–water interface is no longer a boundary and thus requires no additional boundary condition.

The initial condition consists of a zero flow field and an equilibrium interface determined by the force balance between interfacial tension and hydrostatic pressure. The cylinder is partially wetted by the water to form a symmetric dimple, whose

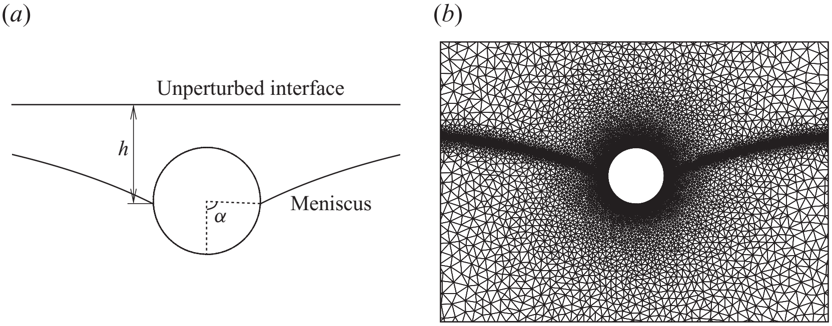

FIGURE 2. (*a*) Schematic of the initial menisci. (*b*) Typical mesh with local refinement around the cylinder and the interface.

lateral extent is characterized by the capillary length:

$$\ell_c = \sqrt{\frac{\sigma}{(\rho_1 - \rho_2)g}}. \tag{2.13}$$

For the 2-D problem considered, the meniscus profile can be obtained analytically (de Gennes *et al.* 2002; Liu, Feng & Wang 2007):

$$x = x_0 \pm \left[\ell_c \cosh^{-1}(-2\ell_c/y) - \sqrt{4\ell_c^2 - y^2} + x_c\right], \tag{2.14}$$

with ± denoting the two symmetric menisci at either side of the cylinder (figure 2*a*). The constant $x_c$ is determined by using the wetting condition at the contact line:

$$x_c = \tfrac{1}{2}D\sin\alpha - \cosh^{-1}(2\ell_c/h) + \sqrt{4\ell_c^2 - h^2}, \tag{2.15}$$

where $D$ is the diameter of the cylinder; $2\alpha$ is the central angle extended by the wetted portion of the cylinder; and $h$ is the vertical distance between the contact line and the unperturbed interface, as illustrated in figure 2(*a*); $h$ and $\alpha$ can be easily obtained by solving $h = \ell_c\sqrt{2[1 + \cos(\theta + \alpha)]}$ and $(1/2)D\cos\alpha - h = y_0$.

To avoid the difficulty associated with the moving solid boundary, the initial-value problem is transformed to a non-inertial frame of reference fixed on the cylinder. Accordingly, the initial and boundary conditions are properly modified, and an appropriate body force is added to the momentum equation. The initial-value problem is numerically solved in a rectangular domain of size $60\ell_c \times 25\ell_c$. Initially the cylinder is $30\ell_c$ from both the left and right bounds of the domain, $10\ell_c$ from the upper bound and $15\ell_c$ from the lower one. A finite-element package AMPHI, which employs unstructured triangle elements and adaptive meshing, is used to solve the governing equations. Details of the algorithm and its validation can be found in Yue *et al.* (2006) and Zhou, Yue & Feng (2010). The mesh is locally refined around the cylinder to capture the boundary layer and around the interface to resolve the phase-field variable, as illustrated in figure 2(*b*).

## 3. Results and discussion

We use $\ell_c$ as the characteristic length and the mean velocity $U_m = 2A/T$ as the characteristic velocity. Then the problem is governed by the following dimensionless groups:

$$\left.\begin{array}{l} Oh = \dfrac{\mu_1}{\sqrt{\rho_1 \sigma \ell_c}}, \quad We = \dfrac{\rho_1 U_m^2 \ell_c}{\sigma}, \quad \theta, \\ \dfrac{\rho_1}{\rho_2}, \quad \dfrac{\mu_1}{\mu_2}, \quad Cn = \dfrac{\epsilon}{\ell_c}, \quad S = \dfrac{\sqrt{\gamma \mu^*}}{\ell_c}, \end{array}\right\} \tag{3.1}$$

together with four length ratios: $D/\ell_c$, $A/\ell_c$, $Y_{max}/\ell_c$ and $Y_{min}/\ell_c$. The Ohnesorge number $Oh$ measures the strength of viscous force with respect to inertial force and interfacial tension. The Weber number $We$ measures the relative importance of inertia to interfacial tension. The Cahn number $Cn$ characterizes the dimensionless interfacial thickness. The parameter $S$, defined with $\mu^* = \sqrt{\mu_1 \mu_2}$, represents the dimensionless Cahn–Hilliard diffusion length, which is a counterpart of the slip length commonly employed in sharp-interface models for moving contact lines (Cox 1986; Yue *et al.* 2010).

An advantage of the above dimensionless numbers is that the driving velocity $U_m$ and the leg diameter $D$ appear only in $We$ and $D/\ell_c$, respectively. Thus $Oh$ is a material constant independent of the specific water walkers. The use of $We$ is appropriate because the propulsive dynamics is dominated by inertia and interfacial tension. One can alternatively use the Reynolds number $Re = \rho_1 U_m \ell_c / \mu_1$ or the capillary number $Ca = \mu_1 U_m / \sigma$, which are related to $Oh$ and $We$ by $Re = \sqrt{We}/Oh$ and $Ca = Oh\sqrt{We}$. Furthermore, the ratio $D/\ell_c$ is related to the Bond number $Bo = (\rho_1 - \rho_2) g D^2 / \sigma$ by $D/\ell_c = \sqrt{Bo}$.

For an air–water system, the dimensional parameters are $\sigma = 72\ \mathrm{dyn\,cm^{-1}}$, $\rho_1 = 10^3\ \mathrm{kg\,m^{-3}}$, $\mu_1 = 8.9 \times 10^{-4}\ \mathrm{Pa\,s}$, $g = 9.8\ \mathrm{m\,s^{-2}}$, $\rho_2 = 1.2\ \mathrm{kg\,m^{-3}}$ and $\mu_2 = 1.78 \times 10^{-5}\ \mathrm{Pa\,s}$, leading to $\ell_c = 2.7\,\mathrm{mm}$. These parameters give $Oh = 2.0 \times 10^{-3}$ and $\mu_1/\mu_2 = 50$, which are used in all calculations. The large density ratio ($\rho_1/\rho_2 \approx 800$) would cause serious errors in the diffuse-interface representation of the component densities. Thus we have used $\rho_1/\rho_2 = 50$ in the calculations; it is large enough so that the inertia of air flow has a negligible effect (cf. figure 3), as is the case in reality. In addition, we choose $S = 0.01$, assuming a diffusion length much smaller than the macroscopic length scale of the problem. Note that the effect of decreasing the value of $S$ is to reduce the contact-line speed (Yue *et al.* 2010). We have used $A = 2\ell_c$ so that the horizontal displacement of the leg is approximately 1.1 cm, comparable to the body lengths of water striders and fishing spiders studied in prior experiments (Suter *et al.* 1997; Hu *et al.* 2003). For water walkers, the characteristic velocity of the rowing leg is typically a few tens of centimetres per second (Suter *et al.* 1997; Suter & Wildman 1999; Hu 2006), corresponding to $We \sim O(1)$. Our simulations will cover the range $0.5 \leqslant We \leqslant 4$. Note that a leg velocity $U_m$ equal to the minimum wave speed $c_{min} = 23\,\mathrm{cm\,s^{-1}}$ gives $We = 1.9$.

The numerical simulations allow us to calculate directly the propulsive force acting on the leg:

$$\boldsymbol{F} = \int_{\Sigma} p\boldsymbol{n}\,\mathrm{d}S - \int_{\Sigma} \mu[\nabla\boldsymbol{v} + (\nabla\boldsymbol{v})^{\mathrm{T}}] \cdot \boldsymbol{n}\,\mathrm{d}S - \int_{C} \sigma\boldsymbol{t}\,\mathrm{d}C, \tag{3.2}$$

where $\Sigma$ is the leg surface; $C$ denotes the contact lines; and $\boldsymbol{t}$ is the unit vector normal to the contact line and lying in the interface. The three terms on the right-hand side denote the contributions of pressure, viscosity and interfacial tension, respectively. Both $\boldsymbol{n}$ and $\boldsymbol{t}$ are defined so that they point from the fluid into the cylinder. We have

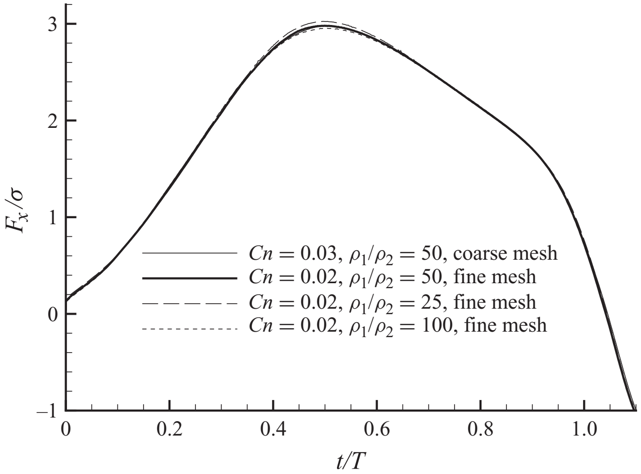

FIGURE 3. Physical and numerical convergence of the time evolution of the horizontal force $F_x$ with respect to the interface thickness and the mesh resolution. The coarse and fine meshes have approximately $7.6 \times 10^4$ and $1.5 \times 10^5$ elements. The dimensionless numbers are $We = 3$ ($Re = 866$), $D/\ell_c = 0.5$, $Y_{max}/\ell_c = 0.1$, $Y_{min}/\ell_c = -0.5$ and $\theta = 120°$. The curves for different values of $\rho_1/\rho_2$ confirm that the density ratio is large enough to represent the air–water system.

adopted the 2-D version of this formula, which gives the force per unit length of the cylinder with two components, $F_x$ and $F_y$. Note that the available curvature force is always less than $2\sigma$.

### 3.1. *Sharp-interface limit*

Diffuse-interface simulations must achieve both physical and numerical convergence to produce reliable results (Zhou *et al.* 2010). Physical convergence requires that the diffuse-interface framework be consistent with the classical Navier–Stokes description with sharp interfaces (Caginalp & Chen 1998). Specifically, the thickness of the diffuse interface should be sufficiently small, i.e. $Cn \ll 1$, so that the diffuse-interface computations converge to the sharp-interface limit. For problems with moving contact lines, Yue *et al.* (2010) demonstrated that this should be achieved by decreasing $Cn$ while keeping $S$ fixed and further presented a convergence criterion $Cn < 4S$, which is followed in our calculations. Numerical convergence is more straightforward; the solution must be adequately resolved and be independent of the mesh size. In general, about 10 grid points are required inside the diffuse interface to adequately resolve the steep variation of $\phi$ (Yue *et al.* 2006). This requires local refinement of the mesh to an element size of about $0.5\epsilon$ at the interface. Furthermore, a comparable mesh size is used around the cylinder to capture the boundary layer at Reynolds numbers up to 1000.

The convergence of the numerical results is illustrated in figure 3 by plotting the time history of $F_x$ for a typical set of parameters. Here we have used $We = 3$, corresponding to $Re = 866$, which is high enough to produce a thin boundary layer. The thin solid curve calculated at $Cn = 0.03$ on a coarse mesh can hardly be distinguished from the thick solid curve for $Cn = 0.02$ on a finer mesh with approximately double the number of elements. To ensure sufficient accuracy, the results presented below were computed using $Cn = 0.02$ on the finer mesh. The figure also depicts computations using different air densities, with $\rho_1/\rho_2$ ranging from 25 to 100, and confirms that $\rho_1/\rho_2 = 50$ is sufficiently large.

### 3.2. *Flow field and hydrodynamic force*

We first present two typical simulations, at $We = 0.5$ and 2.5 corresponding to $Re = 354$ and 791 respectively, to give a general impression of the dynamic process. The diameter of the cylinder $D = 0.5\ell_c = 1.35\,\text{mm}$ is comparable to the real values for fishing spiders (Suter *et al.* 1997). The legs of water walkers are generally hydrophobic, but the contact angle varies considerably (Bush *et al.* 2007). Here we use a typical value $\theta = 120^\circ$; a parametric study on the effect of $\theta$ will be presented later. Geometric parameters for the stroke are given plausible values, since no quantitative data are available: $A = 2\ell_c$, $Y_{max} = 0.1\ell_c$ and $Y_{min} = -0.5\ell_c$. For $We = 0.5$, the mean stroke velocity $U_m$ is well below $c_{min}$, while for $We = 2.5$, it is above it. Figure 4 depicts the stroke, using snapshots of the interface and contours of the vorticity $\omega = \partial v/\partial x - \partial u/\partial y$ in the water. Two prominent features of the process are the vortices and interfacial waves.

At $We = 0.5$ (figure 4*a*), the backward driving stroke creates a counterclockwise (positive) vortex, which detaches from the cylinder at the end of the stroke ($t = 1.01T$). The start of the recovery stroke produces a weaker clockwise vortex, which is easily shed with the help of the first vortex ($t = 1.5T$). The two vortices form a dipole that rotates counterclockwise as a whole and moves downward ($t = 2T$). In the meantime, the cylinder moves forward in the recovery stroke and generates a negative vortex streak under the water surface ($t = 1.5T \sim 2T$). At the higher $We = 2.5$ (figure 4*b*), several new features emerge. The initial positive vortex streak is so strong that it breaks up into several smaller vortices ($t = 1.1T$). Shortly into the recovery stroke, the leg detaches from the interface ($t = 1.3T$) and thus produces no more negative vorticity in the water. The initial positive vortices manage to capture weak negative vortices generated prior to the detachment. They interact with one another in a complex vortical structure and as a whole move to the lower left ($t = 2.1T$). By this time, the leg has reattached to the water surface. The leg detachment and reattachment have been documented for real water striders (Hu & Bush 2010). Note that the 2-D vortex structures are topologically different from the hemispherical vortex dipoles observed in the wake of real water-walking creatures (Hu *et al.* 2003). This difference will be further discussed later.

At both $We$ values, the driving stroke generates a surface wave that propagates to the left. The motion of the leg induces a high pressure to its left, which raises the meniscus into a hump and renders the dimple asymmetric (e.g. figure 4*b*, $t = 0.5T$). The magnitude of the wave increases with $We$ or the stroking velocity. The generation of capillary waves by water walkers is a topic of some controversy in the literature. For example, Suter *et al.* (1997) moved the leg of a fishing spider at constant velocity and saw no waves when this velocity was below $c_{min}$. On the other hand, Hu *et al.* (2003) found that infant striders can produce capillary waves even though their speed is below $c_{min}$. This has been resolved by recognizing the transient nature of the stroke in actual insect propulsion (Hu & Bush 2010). For comparison, we have measured a maximum wave crest $a_{max} = 0.8\,\text{mm}$ and a phase speed $c = 25\,\text{cm s}^{-1}$ at $We = 0.5$ and $a_{max} = 2.8\,\text{mm}$ and $c = 31\,\text{cm s}^{-1}$ at $We = 2.5$. Here $c$ is estimated by following the wave crest in time. Furthermore, the waves are damped in time because of viscous dissipation. For instance, the wave crest has come down to $a = 0.26\,\text{mm}$ by $t = 2T$ for $We = 0.5$. These values are comparable to the experimental measurements of Hu *et al.* (2003) with $a = 0.1 \sim 0.5\,\text{mm}$ and $c \approx 30\,\text{cm s}^{-1}$, although the experimental $We$ was not given.

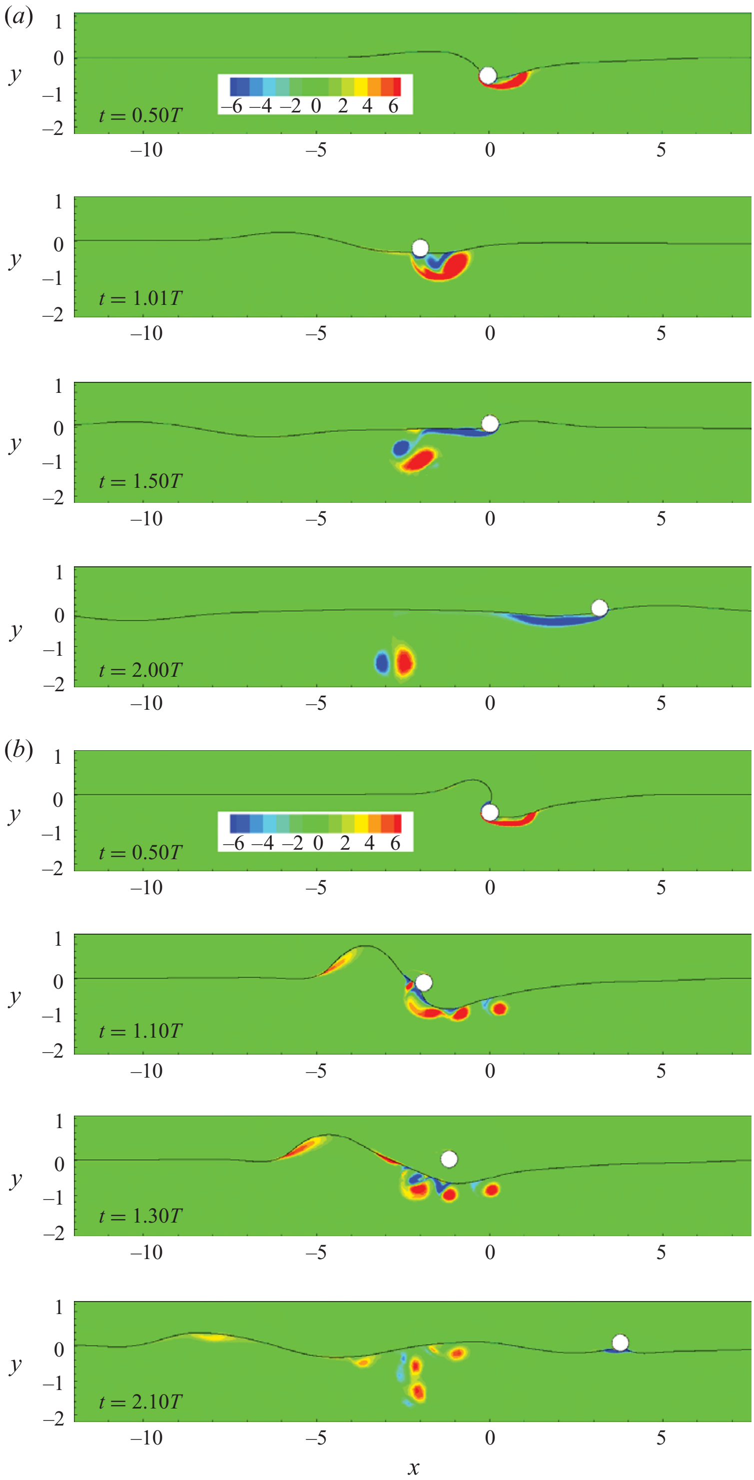

FIGURE 4. Snapshots of the vorticity contours in the water normalized by $U_m/\ell_c$ for (*a*) $We = 0.5$ ($Re = 354$) and (*b*) $We = 2.5$ ($Re = 791$). The solid curves represent the interface. The other parameters are $D/\ell_c = 0.5$, $Y_{max}/\ell_c = 0.1$, $Y_{min}/\ell_c = -0.5$ and $\theta = 120°$.

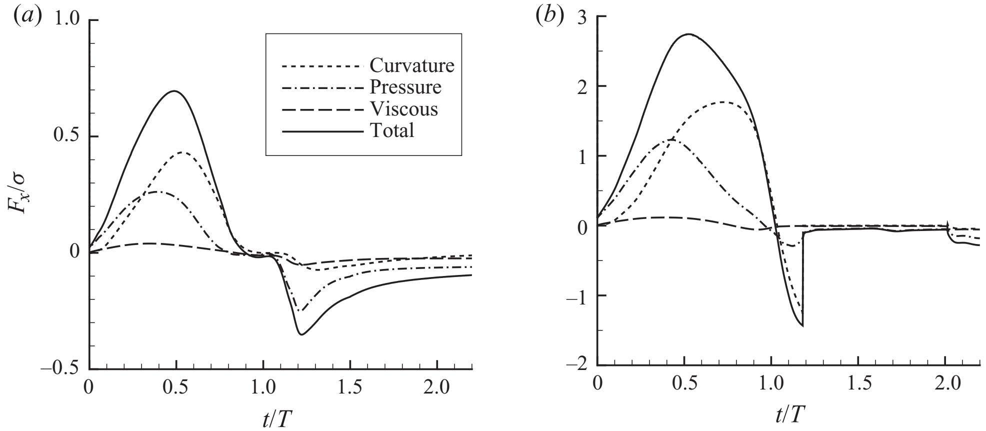

FIGURE 5. Time history of the horizontal force $F_x$ and its components due to curvature, pressure and viscosity during the stroke cycle of figure 4: (*a*) $We = 0.5$; (*b*) $We = 2.5$.

Figure 5 plots the instantaneous horizontal forces $F_x$ for the stroke cycle together with the three contributions to it (cf. (3.2)). For both *We* values, the viscous force is negligible, and $F_x$ is mainly due to the curvature force and the pressure force, which arise from the aforementioned dimple asymmetry and pressure difference, respectively. Moreover, the curvature force is more important than the pressure force in the driving stroke ($0 < t < T$) and is the most responsible for the propulsion of the water walker. This is consistent with the scaling argument of Bush & Hu (2006) on the curvature force. The total force changes sign at the end of the driving phase and remains negative during the recovery phase when it acts as a resistance to the insect's forward motion. At low *We*, this resistance can reach a magnitude comparable to that of the positive thrust and is thus highly undesirable (figure 5*a*). This effect can be suppressed by raising *We* to encourage detachment of the leg from the interface during the recovery stroke (figure 5*b*). The interface becomes so tilted at the end of the driving stroke ($t = 1.1T$ in figure 4*b*) that it readily detaches from the hydrophobic leg. Upon reattachment at $t = 2T$, the leg experiences a slight increase of the resistance. In addition, the faster stroke produces greater propulsive force in the driving phase. Therefore, increasing the stroke velocity is a good strategy for the water walker. We also tested the alternative strategy of raising the leg higher during recovery, up to $Y_{max} = 0.4\ell_c$. But this turns out to be ineffective in producing detachment.

The total vertical force $F_y$ is shown in figure 6. While the driving legs are used for propulsion, their capability for supporting the insect's weight is suppressed except in the early stage of the stroke. The motion of the driving legs results in a decrease of the vertical force, which even turns negative briefly at the start of the recovery stroke as the water walker raises the leg. Fortunately, water walkers use their non-stroking, typically fore and hind, legs to stay afloat while they move.

### 3.3. *Momentum transfer*

Since both waves and vortices are produced by water walkers, it is of interest to quantify how much each contributes to the propulsion. This can be assessed from the horizontal momentum of the two flow structures. We have to note the inherent ambiguity in partitioning the total momentum into one part due to waves and another due to vortices. The regions that visually constitute the waves and the vortices merge into each other smoothly, and a spatial division is of necessity arbitrary. Nevertheless,

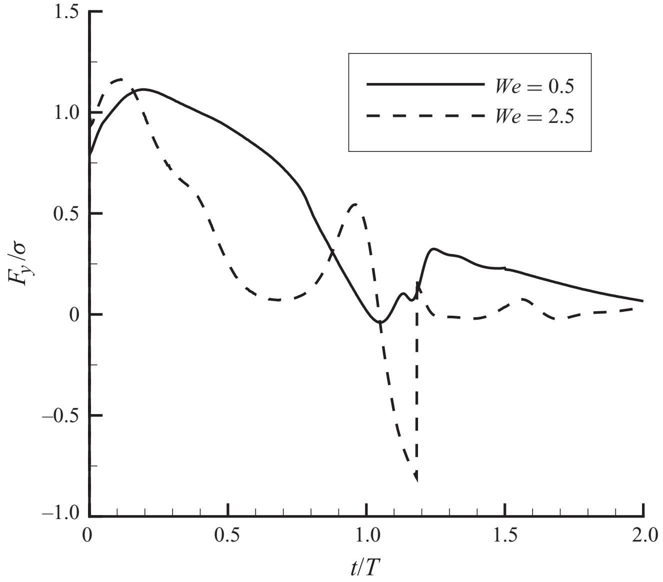

FIGURE 6. Time history of the vertical total force $F_y$ for $We = 0.5$ and 2.5. The other parameters are the same as in figure 4.

under certain circumstances the two structures are distinctly apart, and one can make meaningful statements about their separate contributions to propulsion. One such case, albeit highly idealized, is the flow induced by an impulsive point force, where advection is absent, and a linear theory can be used to calculate the wave and vortex contributions of momentum (Bühler 2007). Another case is the late stage of the rowing stroke for water striders, where, as experimentally observed by Hu *et al.* (2003), the waves and the vortices are well separated in space and are travelling at different velocities.

Hu *et al.* (2003) found that the vortical structures generated by water striders approximate hemispherical dipolar vortices and estimated the vortex contribution to propulsion by computing the momentum of the fluid enclosed in the dipole. In addition, the momentum carried by the waves was calculated using the slowly varying wavetrain theory. Their results suggest that the insect transfers momentum to water mostly through the vortices, and the waves contribute only about 5 % to the propulsion. Bühler (2007) questioned the use of an essentially steady wave theory for estimating the momentum of unsteady waves. By simplifying the leg stroke into an impulsive point force, his calculation attributes two thirds of the momentum to vortices and one third to waves.

In our simulations, distinct vortex and wave regions can be defined in the late stage of the stroke (cf. figure 4). Figure 7 shows a typical picture of the instantaneous vorticity contours and the streamlines at $We = 2$ ($Re = 707$), $D/\ell_c = 0.5$, $Y_{max}/\ell_c = 0.3$, $Y_{min}/\ell_c = -0.5$ and $\theta = 120°$. We define the vortex region as the rectangle $-5 \leqslant x \leqslant 0$ and $-3 \leqslant y \leqslant 0$ that contains the pair of vortices and have computed the vortex contribution to the total momentum directly. The vortex region contains a horizontal momentum of $-0.45\rho_1 U_m \ell_c^2$ out of $-1.42\rho_1 U_m \ell_c^2$ in the whole domain. The negative signs indicate that the water is being pushed backward, while the leg receives a positive propulsive force. Therefore, the vortices carry about one third of the total momentum and hence play a secondary role, while the waves contribute the most to the propulsion.

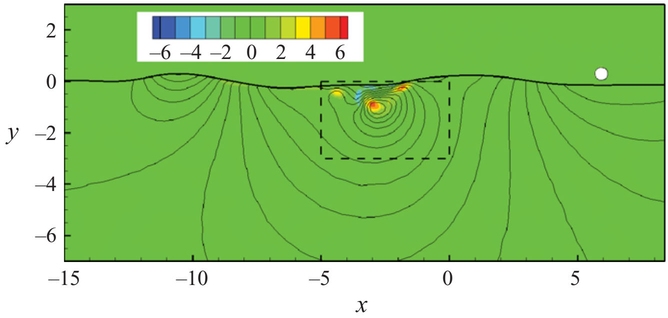

FIGURE 7. Instantaneous streamlines and vorticity contours in water at $t = 2.44T$, $We = 2$ ($Re = 707$), $D/\ell_c = 0.5$, $Y_{max}/\ell_c = 0.3$, $Y_{min}/\ell_c = -0.5$ and $\theta = 120°$. The interval of the streamline contours is $0.06U_m\ell_c$. The thick line represents the interface, and the rectangular box contains the 'vortex' for the purpose of estimating its momentum.

The above findings seem to disagree with the experiment of Hu *et al.* (2003), who found the hemispherical vortices, rather than waves, to be the dominant mechanism of momentum transfer (see figure 3 therein). This discrepancy has to do with the two-dimensionality of our model. Our simulations show vortex pairs with the axis of vorticity parallel to the leg (cf. figure 4); these have a different origin from the hemispherical vortex dipoles of Hu *et al.* (2003). The experiment used small water striders *Gerris remigis* (length $\sim$ 1 cm), and the segment of the leg in contact with water was very short ($\sim$0.1 cm) (Hu & Bush 2010). This produces a 3-D dimple, and the stroke generates a 3-D vortex dipole resembling half of Hill's spherical vortex. As is well known, such a vortex dipole travels with a self-induced velocity and is therefore efficient in transferring momentum (Batchelor 2000). When the wetted portion of the leg is long, as for adult water striders and fishing spiders, it becomes more difficult to produce vortex dipoles that travel at appreciable speed. The dimple is now essentially 2-D as envisioned in our simulation. The start of the leg will generate a pair of counter-rotating vortices at the ends of the dimple, with the vorticity vector perpendicular to the interface. Being far apart, the mutual induction between the two would be weak and inefficient as a momentum carrier. Our 2-D simulations are closer to this picture, and the absence of the hemispherical dipolar vortices leaves the capillary waves as the main mechanism of momentum transfer. On the basis of this analysis, one may expect the larger water walkers to rely more on waves for propulsion and smaller ones on vortices. A more definite understanding will emerge from 3-D computations and laboratory measurements on water walkers of various sizes.

### 3.4. *Effect of We*

A more detailed parametric study is performed to examine the effect of the driving velocity on the propulsive force. The Weber number is varied from 0.5 to 4, and the corresponding $Re$ range is $354 \leqslant Re \leqslant 1000$. A larger $We$ indicates stronger inertia relative to the interfacial tension. Generally, this causes more distortion of the dimple and a stronger propulsion force during the driving stroke. Figure 8 plots the history of the instantaneous horizontal force for different $We$ values and $A/\ell_c = 2$, $D/\ell_c = 0.5$, $Y_{max}/\ell_c = 0.1$, $Y_{min}/\ell_c = -0.5$ and $\theta = 120°$. For $We = 2$ and higher, the leg detaches from the interface in the recovery phase at roughly the same location of the trajectory ($t \approx 1.2T$) for the parameters used here. Similarly, the force curves all peak around $t = 0.5T$, when the leg attains maximum depth and maximum velocity. Since $We$ is

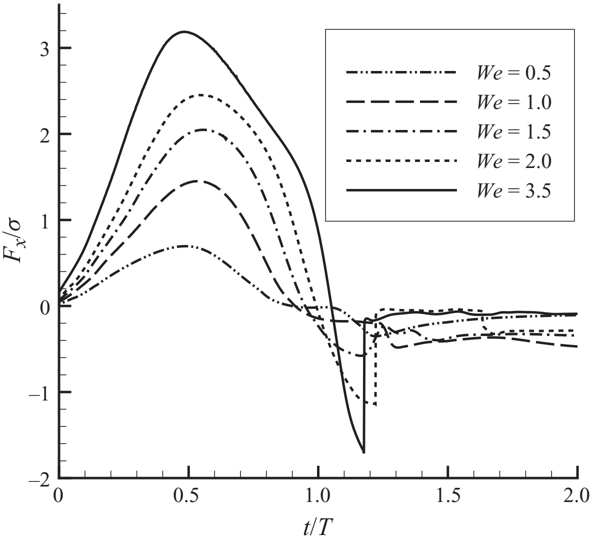

FIGURE 8. Time history of $F_x$ at $We = 0.5$, 1.0, 1.5, 2.0 and 3.5, corresponding to $Re = 354$, 500, 612, 707 and 935, respectively. The other parameters are $A/\ell_c = 2$, $D/\ell_c = 0.5$, $Y_{max}/\ell_c = 0.1$, $Y_{min}/\ell_c = -0.5$ and $\theta = 120°$.

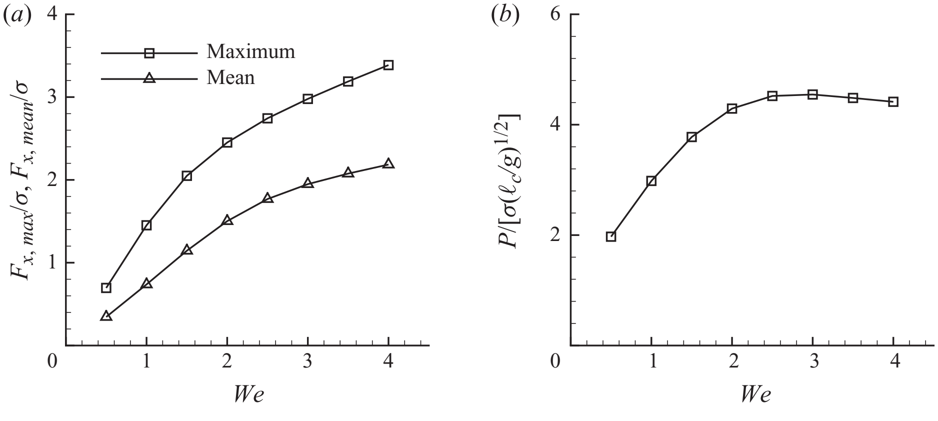

FIGURE 9. (a) The maximum and mean values of $F_x$ as a function of $We$. (b) Impulse of the horizontal force, $P = \int_0^T F_x(t)\,\mathrm{d}t$, as a function of $We$; $P$ is scaled by $\sigma\sqrt{\ell_c/g}$, which is independent of the driving velocity. The other parameters are $A/\ell_c = 2$, $D/\ell_c = 0.5$, $Y_{max}/\ell_c = 0.1$, $Y_{min}/\ell_c = -0.5$ and $\theta = 120°$. The corresponding $Re$ ranges from 354 to 1000.

varied through the mean stroke velocity $U_m = 2A/T$, the actual duration of the stroke is shorter for higher $We$.

Figure 9(a) plots the maximum and mean values of the propulsive force, $F_{x,max}$ and $F_{x,mean} = (1/T)\int_0^T F_x(t)\,\mathrm{d}t$, as functions of $We$. Both increase monotonically with $We$. Note also that the mean force varies linearly with $We$ for $We < 2$, which suggests a quadratic dependence of the mean force on $U_m$. In their experiments, Suter *et al.* (1997) dragged a leg segment at a constant velocity $U$ on the water surface and found a similar relationship $F \sim U^n$ with $1.6 < n < 2.1$ when $U < c_{min}$. This is consistent with our numerical results, although we use a transient stroke model here. Moreover, the force curves are smooth across $We = 1.9$, corresponding to $U_m = c_{min}$, showing no

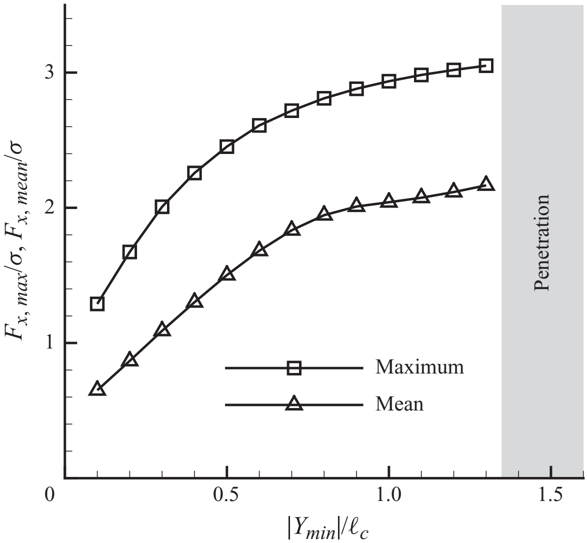

FIGURE 10. The maximum and mean values of $F_x$ as a function of $Y_{min}$ for $We = 2$ ($Re = 707$), $D/\ell_c = 0.5$, $Y_{max}/\ell_c = 0.1$ and $\theta = 120°$. The leg penetrates into the water when $Y_{min} < -1.3\ell_c$.

special effect when the minimum wave speed is exceeded and belying the argument in Denny's paradox (Denny 1993). This is owing to the transient nature of the stroke.

It is also of interest to consider the total impulse of the propulsive force in the driving stroke, $P = \int_0^T F_x(t)\,\mathrm{d}t$, which is related to the momentum gained by the water walker at the end of the stroke. Figure 9(*b*) shows that unlike the mean force $F_{x,mean}$, $P$ does not increase with $We$ monotonically but reaches a maximum at $We = 3$. For higher $We$, $P$ declines slightly, even though $F_{x,mean}$ continues to grow. This is due to the shorter duration of the stroke at higher velocity $U_m$, since the leg displacement $A$ is fixed. Therefore, the insect cannot gain more speed per stroke by rowing faster. It may accelerate more rapidly, of course, by performing more strokes per unit time. We have used the maximum impulse to estimate the locomotion velocity of a fishing spider with typical mass $m = 0.3$ g and leg length $L = 14.5$ mm (Suter *et al.* 1997; Suter & Wildman 1999). With one pair of legs rowing, the maximum velocity attainable is $V = 2PL/m = 0.52\,\mathrm{m\,s^{-1}}$, comparable to the peak velocity ($0.12$–$0.56\,\mathrm{m\,s^{-1}}$) recorded experimentally (Suter & Wildman 1999). Water striders are much lighter ($m \sim 0.01$ g) and can reach speeds as high as $1.5\,\mathrm{m\,s^{-1}}$ (Hu *et al.* 2003). We cannot do a quantitative comparison with this, since our simulations are for a leg diameter $D = 0.5\ell_c$, appropriate for fishing spiders but much too thick for water striders.

### 3.5. *Effect of depth of stroke*

To generate a larger propulsive force, water walkers may sweep their legs deeper into the water during the driving stroke, in addition to rowing the legs faster. Figure 10 shows the propulsive force as a function of the maximum depth of the driving leg $|Y_{min}|$ at $We = 2$ ($Re = 707$), $D/\ell_c = 0.5$, $Y_{max}/\ell_c = 0.1$ and $\theta = 120°$. A larger value of $|Y_{min}|$ corresponds to a deeper dimple, which may be distorted more by a stroke at the same speed, leading to a larger curvature force and hence a larger total thrust. Alternatively, water walkers can use a slower but deeper stroke to produce a similar amount of propulsive force. Note the remarkable similarity between figures 9 and 10.

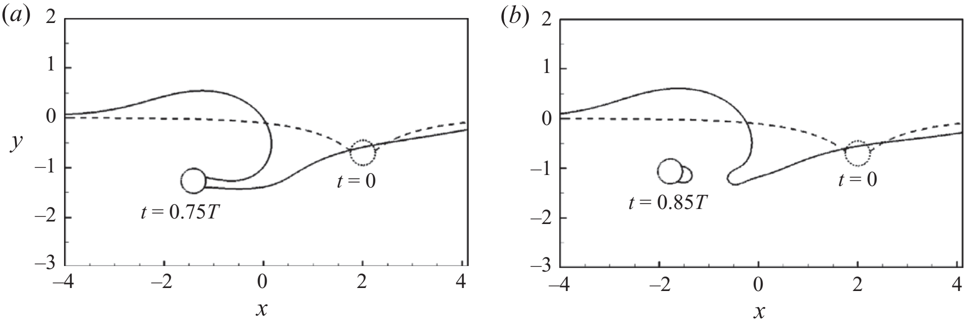

FIGURE 11. An example of interface penetration at $We = 2$ ($Re = 707$), $D/\ell_c = 0.5$, $Y_{max}/\ell_c = 0.1$, $Y_{min}/\ell_c = -1.5$ and $\theta = 120°$. The initial positions of the leg and the interface are represented by the dashed curves for reference.

However, a deep stroke carries the peril that the interface might be pierced by the leg, as illustrated in figure 11 for $Y_{min} = -1.5\ell_c$. Physically, the integrity of the dimple or the interface is maintained by the balance between the capillary pressure ($\sim\sigma/|Y_{min}|$) and the dynamic pressure ($\sim\rho U_m^2$). When the leg is deep enough ($Y_{min} < -1.3\ell_c$ for the parameters in figure 10), the capillary pressure becomes too small to withstand the dynamic pressure under the meniscus, leading to interface penetration. This occurs through the pinch-off of an elongated finger of air (figure 11*a*) and leaves a small bubble attached to the leg (figure 11*b*). This forms an interesting contrast to the detachment of the leg from the interface as in figure 4(*b*), where the two contact lines merge before detachment. Upon rupture of the air finger, the curvature force is no longer available for the leg–bubble system, or equivalently, the curvature force acting on the leg is cancelled out by the capillary pressure inside the bubble. As a consequence, the propulsive force drops abruptly, and the locomotion will be arrested. This puts a limit on the maximum depth of the stroke.

Using a fishing-spider leg dragged at constant speed over the water interface, Suter & Wildman (1999) observed a linear increase in the propulsion force with the depth of the cylinder and a drastic decrease of the force upon penetration. Figure 10 shows a similar linear dependence up to $|Y_{min}| \approx 0.7\ell_c$. The experimental observation that the critical depth decreases with the velocity of the leg is also consistent with our scaling argument above. More quantitative comparisons are hampered by geometric differences between the real spider leg and our circular cylinder. The spider leg tapers from 1.5 to 0.5 mm and is in general thinner than our cylinder ($D = 1.35$ mm). Furthermore, the leg segment is not straight and makes a dimple much shorter than the leg itself. These may explain the measured force being several times smaller than the computed value. The thinner leg also penetrates the water at smaller depth than computed. At $We = 2$, for example, penetration occurs at a depth of 2.3 mm in the experiment, compared with $1.3\ell_c \approx 3.5$ mm in figure 10.

### 3.6. *Effect of contact angle*

The results discussed so far are for $\theta = 120°$. We have also varied the wettability of the cylinder from hydrophilic to super-hydrophobic, with $\theta$ ranging from 60° to 150°. The effect on the propulsive force is depicted in figure 12 for $We = 2$ ($Re = 707$), $D/\ell_c = 0.5$, $Y_{max}/\ell_c = 0.2$ and $Y_{min}/\ell_c = -0.5$. Perhaps surprisingly, the propulsive force during the driving stroke is insensitive to the contact angle; a larger $\theta$ leads to only a slight increase of the maximum force, while the mean force remains essentially constant

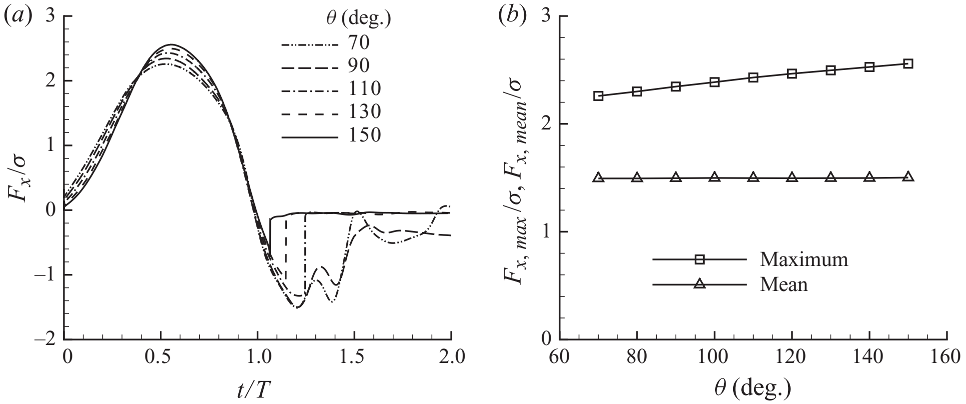

FIGURE 12. (*a*) Time history of $F_x$ for different values of $\theta$. (*b*) The maximum and mean values of $F_x$ as a function of $\theta$. The other parameters are $We = 2$ ($Re = 707$), $D/\ell_c = 0.5$, $Y_{max}/\ell_c = 0.2$ and $Y_{min}/\ell_c = -0.5$.

(figure 12*b*). When the interface is plotted at the same $t$ for different $\theta$ values (not shown here), the meniscus differs slightly and only close to the leg, and apparently intersects the leg at the same slope. Thus, the meniscus is also insensitive to the contact angle $\theta$. This is especially true for thin legs.

The above observations can be rationalized by an analogy to the static case of a hydrophobic cylinder floating on a water surface. Insofar as the buoyant weight of the cylinder is carried by the interface at the contact lines, the slope of the interface there changes little with $\theta$ (Vella *et al.* 2006; Liu *et al.* 2007). Varying $\theta$ shifts the contact line along the cylinder without significantly modifying the meniscus. In the driving stroke, the meniscus is deformed by the dynamic water pressure underneath the surface. As long as the leg moves with the same trajectory and speed, the dynamic pressure is roughly the same. The differing $\theta$ is reflected only by small shifts of the contact line. Thus, the pressure and curvature forces on the cylinder are mostly unaffected, and so is the total $F_{x,mean}$ in figure 12(*b*).

Although the water repellency of the leg is not essential for producing the propulsive force, it plays an important role in the recovery phase. A hydrophilic cylinder does not detach from the interface ($\theta \leqslant 90^\circ$ in figure 12*a*) and incurs a large resistance. Hydrophobicity helps the water walker detach its rowing leg from the water, and do so earlier in the recovery phase for larger contact angles. The mechanism of super-hydrophobicity promoting detachment has also been observed in the experiment of Lee & Kim (2009). They found that lifting a super-hydrophobic cylinder from the water surface takes much less energy than lifting a hydrophilic one. These authors also found that the same mechanism facilitates the bounce-off of a sphere after it impacts a water surface (Lee & Kim 2008), suggesting a critical role for the leg super-hydrophobicity in the jumping of water walkers.

Another benefit of hydrophobicity is to allow higher rowing speed (*We*) or greater depth ($|Y_{min}|$) before the leg penetrates the interface (cf. figure 10). This increases the safety margin during propulsion in terms of gaining greater thrust without the leg falling under water. For example, with $\theta = 120^\circ$ and $Y_{min} = -0.5\ell_c$, the integrity of the dimple is maintained, with no penetration, up to $We = 4$ (figure 9). With $\theta = 60^\circ$, however, interfacial penetration has already occurred at $We = 2$. It is interesting to note that when a hydrophobic leg becomes fully submerged, it retains an air bubble

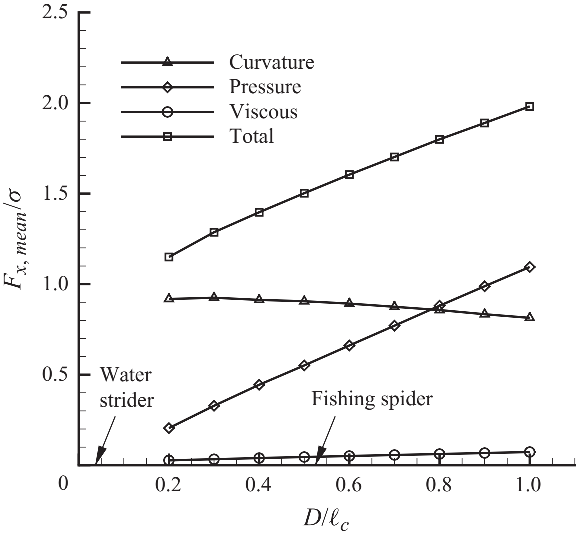

FIGURE 13. The mean propulsive force and its components for a range of leg diameter $D$ at $We = 2$ ($Re = 707$), $Y_{max}/\ell_c = 0.1$, $Y_{min}/\ell_c = -0.5$ and $\theta = 120°$.

(figure 11*b*). On a hydrophilic cylinder, on the other hand, the interface penetration occurs via the merging of the two contact lines, and no air bubble is entrapped.

### 3.7. *Effect of leg diameter*

The leg diameter of water walkers ranges from about 100 μm for water striders to 1.5 mm for fishing spiders (Hu 2006). In our simulations, we have examined the effect of the leg diameter $D$ over the range of $0.2\ell_c \leqslant D \leqslant \ell_c$, or between 0.54 and 2.7 mm in dimensional terms. Simulating thinner legs becomes computationally costly, as it would require a thinner diffuse interface and a smaller $Cn$ to approach the sharp-interface limit. For the $D$ range explored, the physical picture discussed above for the generation of waves, vortices and the propulsive forces remains qualitatively the same. We thus conclude that the same propulsion mechanism is valid for fishing spiders, water striders and other surface-dwelling insects provided that they use a similar rowing gait.

Thick and thin legs do differ in the relative importance of the pressure force and the curvature force in propulsion. Figure 13 shows the mean values of the propulsive force and its three components averaged over the driving stroke as functions of $D$ for $We = 2$ ($Re = 707$), $Y_{max}/\ell_c = 0.1$, $Y_{min}/\ell_c = -0.5$ and $\theta = 120°$. As expected, the pressure force scales linearly with the leg size and tends to zero as $D$ decreases. In contract, the curvature force shows a gradual decrease with increasing $D$. Thus, the pressure force becomes the leading component for thick legs ($D > 0.8\ell_c$), while the curvature force dominates for thinner legs. The legs of water striders are so thin that the propulsive force should be mostly due to the curvature force.

### 3.8. *Discussion*

Compared with prior studies of water-walker locomotion, we have the unique advantage of having detailed numerical data on the flow and stress fields generated by the stroke of the leg. This enables us to construct the following scenario:

(*a*) In the driving stroke, the pressure and curvature forces deform the dimple. In this process, the surface tension effectively joins the meniscus to the leg to form a 'leg-cum-dimple' object, which has a much larger surface area than the leg and drives a much larger mass of water. This produces the propulsive force.

(*b*) This process delivers momentum from the rowing leg to the water, which is later turned into momentum carried by surface waves and subsurface vortices.

(*c*) In the recovery phase of the stroke, the leg would incur friction if it stayed in contact with the surface. Hydrophobicity facilitates the detachment of the leg and enhances the overall efficiency of the propulsion cycle.

This picture reconciles the aforementioned propulsion mechanisms proposed in the literature. First, the form drag idea of Suter *et al.* (1997) is consistent with our stage (*a*), and viewing the leg-cum-dimple as a hull of a vessel is very instructive. In our view, their form drag on the leg-cum-dimple consists of all the three components, i.e. the pressure, curvature and viscous forces, that we find in the driving stroke (cf. figure 5). The form drag on the wetted part of the leg is our pressure force, and the form drag on the meniscus amounts to our curvature force. This is because the surface tension maintains the shape of the meniscus that displaces the water. The dynamic pressure under the meniscus is in effect 'transmitted' to the leg via the curvature force that acts on the contact line. That is how the leg derives a greater thrust from displacing a large amount of water. Note, however, that the experiment of Suter *et al.* (1997) is steady-state and does not probe the later stages of the process.

To the debate between waves and vortices as the main vehicle for propulsion, our results add two insights. First, the driving stroke delivers momentum from the leg to the water via the pressure and curvature forces discussed above. That is the immediate origin of the propulsion force. The partition of water momentum between vortices and waves occurs *later*. Second, this partition has to do with the shape of the leg and the dimple. Our 2-D simulation approximates long legs of larger insects, which produce a slender dimple. In this case, waves are more important than vortices as carriers of momentum. Conversely, short legs produce conical dimples. The rowing of the leg then sheds a dipole of vortices that move at high speed through mutual induction. As clearly documented by Hu *et al.* (2003), this mechanism makes the vortices the dominant player. For long legs, such induction is weaker, and so is the contribution of vortices. Again, in both cases the immediate source of the propulsion is the pressure and curvature forces along the meniscus during the stroke. The present 2-D simulations cannot reproduce the 3-D vortices of Hu *et al.* (2003) nor probe their later development in the wake of small water walkers.

Another interesting result from our simulations is to confirm that the integrity of the dimple sets an upper limit on the magnitude of the thrust that can be generated by the stroke. As Suter *et al.* (1997) demonstrated, the meniscus extends the effective area of the leg and enables the insect to push a larger amount of surrounding water backward. Larger propulsive forces can be achieved with faster and deeper strokes, until the leg penetrates the surface and becomes submerged. Moving a spider leg over a water surface at a constant speed, Suter & Wildman (1999) measured the critical depth of the dimple for penetration as a function of the speed. Although our stroke is unsteady, the trend is the same; the critical rowing depth decreases with rowing speed. In reality, both fishing spiders and water striders are known to occasionally penetrate the water surface (Suter & Wildman 1999; Goodwyn & Fujisaki 2007).

Finally, viscous friction makes a negligible contribution to the propulsion, as clearly shown in figure 5. Indeed, the thrust comes from the inertial force of pushing a large amount of water backward and the interfacial tension acting on the contact lines. In this sense, the propulsion has an inviscid mechanism. Of course, the motion of the contact line is strongly affected by viscosity. For real water walkers, this depends on the microscopic texture of the integument. Viscosity is important on such small length scales.

## 4. Conclusions

We have performed 2-D numerical simulations on the locomotion of water walkers. An unsteady model of the leg motion was employed to mimic the transient behaviour of the rowing stroke. Owing to the unsteadiness, water walkers exploit a time-dependent force-generation mechanism rather than the classical wave drag for propulsion.

During the driving stroke, the dimple moves together with the rowing leg and deforms asymmetrically. The resulting curvature force is the most important component of the thrust. The pressure force plays a major role as well, and the viscous force is negligible. The dominance of the curvature force is especially true for water striders, whose legs are much thinner than the capillary length. In order to increase the propulsive force, water walkers can increase the rowing velocity or the depth of the stroke. However, the integrity of the dimple must be maintained; if the rowing speed or depth becomes too large, the leg pierces the interface and sinks under the water, causing drastic reduction in propulsion. The propulsive force is insensitive to the wetting property of the leg, provided the fluid interface is not penetrated. Hydrophobicity is useful, however, in helping the leg detach from water and thus decreasing the resistance in the recovery stroke. In addition, water repellency of the leg delays interface penetration and makes the propulsion more robust.

We acknowledge support by the Petroleum Research Fund, the Canada Research Chair programme, NSERC (Discovery and Strategic grants) and CFI. We benefited from discussions with Professor He Guowei and Dr Chunfeng Zhou. J.J.F. thanks Professor Shu Chang and the Department of Mechanical Engineering of the National University of Singapore for hosting his sabbatical leave, where part of the work was done.

## REFERENCES

Anderson, N. M. 1976 A comparative study of locomotion on the water surface in semiaquatic bugs (Insects, Hemiptera, Gerromorpha). *Vidensk. Meddr. Dansk. Naturh. Foren.* **139**, 337–396.

Batchelor, G. K. 2000 *An Introduction to Fluid Dynamics*. Cambridge University Press.

Bühler, O. 2007 Impulsive fluid forcing and water strider locomotion. *J. Fluid Mech.* **573**, 211–236.

Bush, J. W. M. & Hu, D. L. 2006 Walking on water: biolocomotion at the interface. *Annu. Rev. Fluid Mech.* **38**, 339–369.

Bush, J. W. M., Hu, D. L. & Prakash, M. 2007 The integument of water-walking arthropods: form and function. *Adv. Insect. Physiol.: Insect. Mech. Control* **34**, 117–192.

Caginalp, G. & Chen, X. F. 1998 Convergence of the phase field model to its sharp interface limits. *Eur. J. Appl. Maths* **9**, 417–445.

Cox, R. G. 1986 The dynamics of the spreading of liquids on a solid surface. Part 1. Viscous flow. *J. Fluid Mech.* **168**, 169–194.

Denny, M. W. 1993 *Air and Water: The Biology and Physics of Life's Media*. Princeton University Press.

Denny, M. W. 2004 Paradox lost: answers and questions about walking on water. *J. Expl Biol.* **207**, 1601–1606.

Dickinson, M. 2003 Animal locomotion: how to walk on water. *Nature* **424**, 621–622.

Gao, X. F. & Jiang, L. 2004 Water-repellent legs of water striders. *Nature* **432**, 36.

de Gennes, P.-G., Quéré, D., Brochard-Wyart, F. & Reisinger, A. 2002 *Capillarity and Wetting Phenomena: Drops, Bubbles, Pearls and Waves*. Springer.

GOODWYN, P. P. & FUJISAKI, K. 2007 Sexual conflicts, loss of flight, and fitness gains in locomotion of polymorphic water striders. *Entomol. Exp. Appl.* **124**, 249–259.

HU, D. L. 2006 Thy hydrodynamics of water-walking insects and spiders. PhD thesis, Massachusetts Institute of Technology, Cambridge, MA.

HU, D. L. & BUSH, J. W. M. 2010 The hydrodynamics of water-walking arthropods. *J. Fluid Mech.* pp. 5–33.

HU, D. L., CHAN, B. & BUSH, J. W. M. 2003 The hydrodynamics of water strider locomotion. *Nature* **424**, 663–666.

HU, D. L., PRAKASH, M., CHAN, B. & BUSH, J. W. M. 2007 Water-walking devices. *Exp. Fluids* **43**, 769–778.

JACQMIN, D. 2000 Contact-line dynamics of a diffuse fluid interface. *J. Fluid Mech.* **402**, 57–88.

KELLER, J. B. 1998 Surface tension force on a partly submerged body. *Phys. Fluids* **10**, 3009–3010.

LAMB, H. 1932 *Hydrodynamics*, 6th edn. Cambridge University Press.

LEE, D. G. & KIM, H. Y. 2008 Impact of a superhydrophobic sphere onto water. *Langmuir* **24**, 142–145.

LEE, D. G. & KIM, H. Y. 2009 The role of superhydrophobicity in the adhesion of a floating cylinder. *J. Fluid Mech.* **624**, 23–32.

LIU, J. L., FENG, X. Q. & WANG, G. F. 2007 Buoyant force and sinking conditions of a hydrophobic thin rod floating on water. *Phys. Rev.* E **76**, 066103.

MANSFIELD, E. H., SEPANGI, H. R. & EASTWOOD, E. A. 1997 Equilibrium and mutual attraction or repulsion of objects supported by surface tension. *Phil. Trans. R. Soc. Lond.* A **355**, 869–919.

QIAN, T. Z., WANG, X. P. & SHENG, P. 2006 A variational approach to moving contact line hydrodynamics. *J. Fluid Mech.* **564**, 333–360.

RAPHAËL, E. & DE GENNES, P. G. 1996 Capillary gravity waves caused by a moving disturbance: wave resistance. *Phys. Rev.* E **53**, 3448–3455.

SONG, Y. S. & SITTI, M. 2007 Surface-tension-driven biologically inspired water strider robots: theory and experiments. *IEEE Trans. Robot.* **23**, 578–589.

SUN, S. M. & KELLER, J. B. 2001 Capillary–gravity wave drag. *Phys. Fluids* **13**, 2146–2151.

SUTER, R. B., ROSENBERG, O., LOEB, S., WILDMAN, H. & LONG, J. H. 1997 Locomotion on the water surface: propulsive mechanisms of the fisher spider *Dolomedes triton. J. Expl Biol.* **200**, 2523–2538.

SUTER, R. B. & WILDMAN, H. 1999 Locomotion on the water surface: hydrodynamic constraints on rowing velocity require a gait change. *J. Expl Biol.* **202**, 2771–2785.

VELLA, D., LEE, D. G. & KIM, H. Y. 2006 The load supported by small floating objects. *Langmuir* **22**, 5979–5981.

YUE, P. T., ZHOU, C. F. & FENG, J. J. 2010 Sharp interface limit of the Cahn–Hilliard model for moving contact lines. *J. Fluid Mech.* **645**, 279–294.

YUE, P. T., ZHOU, C. F., FENG, J. J., OLLIVIER-GOOCH, C. F. & HU, H. H. 2006 Phase-field simulations of interfacial dynamics in viscoelastic fluids using finite elements with adaptive meshing. *J. Comput. Phys.* **219**, 47–67.

ZHOU, C. F., YUE, P. T. & FENG, J. J. 2010 3D phase-field simulations of interfacial dynamics in Newtonian and viscoelastic fluids. *J. Comput. Phys.* **229**, 498–511.